European Journal of Mechanics / A Solids 117 (2026) 105963

Contents lists available at ScienceDirect

European Journal of Mechanics / A Solids

journal homepage: www.elsevier.com/locate/ejmsol

Full Length Article

Influence of the sample shape factor on the dynamic characterization of viscoelastic properties: complex moduli and Poisson's ratio

Julen Cortazar-Noguerol *, Fernando Cortés, María Jesús Elejabarrieta

Department of Mechanics, Design and Industrial Management, University of Deusto, Avda. de las Universidades 24, 48007, Bilbao, Spain

ARTICLE INFO

Keywords:
Complex Poisson's ratio
Complex compressive modulus
Complex shear modulus
Silicone rubber
Shape factor
Torsion test
Compression test

ABSTRACT

This study investigates how the sample shape factor influences the dynamic properties characterization of a silicone rubber within the linear viscoelastic regime. The effective elastic properties of elastomers are known to depend on geometry, but the effect of shape factor on the dynamic response has not been systematically characterized. To address this, cylindrical samples with varying geometries are tested under dynamic compression and torsion. The results reveal that both the complex compressive and shear moduli are affected by shape factor, and that this influence varies with frequency. To quantify the influence of shape factor and extract the material's dynamic properties, a phenomenological correction model is formulated. The model introduces frequency-dependent parameters that account for the geometric effects on the effective moduli. These corrected moduli yield a complex Poisson's ratio that exhibits a slight frequency dependence, with a decreasing real part and an increasing loss factor. This approach enables both the quantification of geometry-induced effects in dynamic mechanical testing and the extraction of intrinsic material's viscoelastic properties.

1. Introduction

Elastomeric materials are widely used in industry applications that require high deformability, energy dissipation, and mechanical stability under cyclic loading (Alarifi, 2023; Yang et al., 2023; Alam, 2024; Bodin et al., 2024; Chakraborti et al., 2025; Zhao et al., 2023). These components are often subjected to mechanical stresses such as compression and shear, to which elastomers respond through viscoelastic mechanisms, resulting in frequency-dependent behavior (Nashif et al., 1985; Jones, 2001; Edwards et al., 2000; Ehrig et al., 2018; Somanath et al., 2023). Characterizing this response is essential for accurate constitutive modeling and reliable performance analysis (Brown, 1996; Annarasa et al., 2020; Adrover-Monserrat et al., 2022; Liu et al., 2023a; Wang et al., 2024). Complex compressive and shear moduli, together with Poisson's ratio, are interrelated and must be considered collectively to ensure consistency with the physical constraints that govern the behavior of isotropic viscoelastic materials (Bower, 2010; Szabó and Babuška, 2021; Lakes and Wineman, 2006; Hilton and Yi, 1998).

Both the complex compressive and shear moduli can be determined using non resonant forced vibration methods (ISO 6721a; ISO 6721b). The complex compressive modulus can be measured using a Dynamic Mechanical Analyzer (DMA) (Zhu and Li, 2021; Li and Sun, 2011; Dynamic Mechanical Analysis, 2009; Pattison et al., 2015; Henriques et al., 2018; Xu and Gupta, 2018; Phansalkar et al., 2025) and the complex shear modulus is usually measured via torsional rheometry (Agirre-Olabide et al., 2014; Agirre-Olabide and Elejabarrieta, 2016; Hancox, 1972; Ahmed, 2009; Jutzeler et al., 2020; Dessi et al., 2021; Asp et al., 2022; Virág et al., 2024) or DMA in pure shear configuration (Pal and Bhattacharyya, 2025; Esmaeeli et al., 2019). Since the viscoelastic response is sensitive to experimental conditions such as temperature, frequency, preload, etc. (Cortazar-Noguerol et al., 2024; Liu et al., 2023b), any valid interrelation between moduli requires that they be obtained under identical testing conditions both in compression and torsion tests (Tschoegl et al., 2002).

Regarding the complex Poisson's ratio, it can be determined via direct or indirect methods (Pritz, 2000; Sousa et al., 2018; Boiko et al., 2010; Sim and Kim, 1990; Smith et al., 2024; Fauser et al., 2025). An existing study employed an axial-torsional rheometer to obtain the dependence of the complex Poisson's ratio on temperature and frequency from tension and torsion testing in clamped cylindrical specimens (Rodríguez Agudo et al., 2023). Moreover, a recent study using the same equipment compares direct and indirect approaches, showing that direct methods, based on measuring axial and lateral strains using strain gauges, provide consistent results for both the real and imaginary

* Corresponding author.
E-mail address: j.cortazar@deusto.es (J. Cortazar-Noguerol).

https://doi.org/10.1016/j.euromechsol.2025.105963
Received 24 July 2025; Received in revised form 24 November 2025; Accepted 27 November 2025
Available online 28 November 2025

components of the complex Poisson's ratio (Fauser et al., 2025). In contrast, the indirect approach, measuring the complex tensile and shear moduli, yielded comparable values for the real part, but the determination of the imaginary component remained inconclusive.

Despite efforts to ensure consistency by matching experimental conditions across compression and torsion tests, the geometry of the sample introduces systematic effects that cannot be ignored. On the one hand, in compression testing of cylindrical samples, the measured modulus increases with shape factor due to lateral confinement, an effect that has been extensively studied and modeled under quasistatic conditions (Brown, 1996; Vatandoost et al., 2021; ISO 7743). In contrast, although it is known that geometry influences the measured dynamic compressive modulus, systematic studies are limited and current models do not account for the combined influence of frequency and geometry (Vatandoost et al., 2021; Yaghoobi et al., 2022; Gordaninejad et al., 2012; Lopes et al., 2020). On the other hand, in torsion testing, no consensus exists regarding the role of specimen geometry either in quasistatic or the dynamic case. Although rod-like samples have been shown to yield more reliable quasistatic shear moduli (Borin et al., 2018), standard rheometry protocols for soft solids (originally developed for fluids and gels) continue to recommend disc-like geometries (ISO 6721b; ISO 3219). On the contrary, those same standards for harder solids (>10 MPa) recommend thin rods as sample geometry (ISO 6721c). In addition, torsion testing presents a methodological trade-off: the specimen must either be bonded to the fixtures (modifying boundary conditions and the measured stiffness) or, if unbonded, wall-slip at the interfaces must be accounted for (Walter et al., 2017a, 2017b). A recent systematic study on the effect of specimen geometry on the shear modulus determination via quasistatic torsion testing demonstrated how rod-like samples are expected to report more realistic results (Cortazar-Noguerol et al., 2025).

To obtain the complex Poisson's ratio from compressive and shear moduli the influence of shape factor on the measured moduli must first be quantified, as has been done for the quasistatic case (Cortazar-Noguerol et al., 2025). Given this gap in literature, the main objective of this work is to quantify and model the influence of the sample geometry on the characterization of the dynamic properties of an elastomer. To this end, a methodology is developed by combining experimental data analysis and phenomenological model curve fitting, based on dynamic compression and torsion tests conducted on cylindrical samples of silicone rubber with varying geometries. A correction model is proposed to account for the influence of geometry on both the complex compression and shear moduli. This model is a generalization of the previously developed quasistatic model (Cortazar-Noguerol et al., 2025), introducing complex frequency-dependent parameters and enabling the computation of the complex Poisson's ratio.

The article is organized as follows. Section 2 introduces the theoretical background and outlines the existing correction models. Section 3 describes the materials, sample preparation, and experimental methods. Section 4 presents experimental results. Section 5 details the parameter identification, corrected moduli, and the computation of Poisson's ratio. Finally, Section 6 summarizes the conclusions and main findings.

2. Theoretical framework

This section begins with a review of the fundamental equations of linear viscoelasticity, with particular focus on the complex moduli obtained from dynamic compression and torsion tests. Next, existing models addressing the influence of sample geometry in quasistatic testing are discussed.

2.1. Linear viscoelastic response in dynamic testing

This subsection summarizes the theoretical basis of linear viscoelastic behavior under dynamic loading in compression and torsion testing. When subjected to harmonic loading, and strain levels within the linear viscoelastic range, the material's behavior can be described using complex moduli (Inman, 2014), which account for both energy storage and dissipation. The complex moduli are defined as complex magnitudes, which can be decomposed into their real and imaginary parts such that

$$M^* = M' + \mathrm{i}M'' = M'(1 + \mathrm{i}\eta_M) \tag{1}$$

where M^* represents any complex modulus (in this work the complex compressive E^* and shear G^* moduli), M' is the storage modulus, which is proportional to the energy stored as an elastic deformation, M'' is the loss modulus and is proportional to the energy loss on each of the oscillations due to viscous dissipation and $\mathrm{i} = \sqrt{-1}$ is the imaginary unit. The ratio between the loss and storage components is the loss factor $\eta_M = M''/M'$, which is related to the phase difference δ_M between the excitation and the response through $\eta_M = \tan\delta_M$. In general, M', M'', and δ_M depend on the frequency of the harmonic loading (Nashif et al., 1985; Jones, 2001).

In isotropic materials, the complex compressive modulus and the shear complex modulus are related through the complex Poisson's ratio such that

$$E^* = 2G^*(1 + \nu^*), \tag{2}$$

where ν^* is the complex Poisson's ratio, which is assumed to be complex for viscoelastic materials (Pritz, 1998, 2000, 2007). An analogous definition to Eq. (1) can be formulated for the complex Poisson's ratio. However, this quantity does not describe a relationship between stress and strain, but a relationship between axial and transversal strains such that

$$\nu^* = -\frac{\varepsilon_T}{\varepsilon_A}\exp[\mathrm{i}(\delta_A - \delta_T)], \tag{3}$$

where ε_A and ε_T are the axial and transversal strain amplitudes respectively and $\delta_A - \delta_T$ is the phase difference between them. In isotropic and homogeneous materials, it is expected for the transversal strain to lag behind the axial strain, therefore, $\delta_A - \delta_T < 0$ and the imaginary part of the complex Poisson's ratio can be defined as negative:

$$\nu^* = \nu' - \mathrm{i}\nu'' = \nu'(1 - \mathrm{i}\eta_\nu), \tag{4}$$

where ν' and ν'' are the real and imaginary part of the complex Poisson's ratio respectively and $\eta_\nu = \nu''/\nu'$ is its loss factor (Pritz, 2007). Unlike the case of complex moduli, the real part, imaginary part, and loss factor of the complex Poisson's ratio are not directly associated with energy storage or dissipation; rather, their complex nature reflects the phase difference between transverse and axial strains. In terms of the complex compressive and shear moduli, the magnitudes defined in Eq. (4) can be written as

$$\nu' = \frac{E'(1 + \eta_E\eta_G)}{2G'(1 + {\eta_G}^2)} - 1, \tag{5}$$

$$\nu'' = \frac{E'(\eta_G - \eta_E)}{2G'(1 + \eta_G^2)} \tag{6}$$

and

$$\eta_\nu = \frac{\eta_G - \eta_E}{1 + \eta_E\eta_G - \frac{2G'}{E'}(1 + \eta_G^2)}. \tag{7}$$

The behavior of the complex Poisson's ratio with frequency is well stablished. In isotropic homogeneous viscoelastic materials its real part is monotonically decreasing while its loss factor has, at least, a maximum (Tschoegl et al., 2002; Pritz, 1998, 2000).

In addition, if the material under study is nearly incompressible, i.e., the real part of the complex Poisson's ratio is near to 0.5, and $\eta_G < 0.3$,

then it can be assumed that (Pritz, 2007)

$$\frac{\eta_\nu}{\eta_G} \approx 1 - 2\nu', \tag{8}$$

which is a convenient equation given it shows that if $\nu' \to 0.5$ then $\eta_\nu \to 0$.

2.2. Influence of geometry and correction models

Standards for the obtention of the compressive modulus in quasi-static regime point out that the shape of the sample can affects the measured results (ISO 7743). For nearly incompressible elastomers, friction or bonding at the platens suppresses radial expansion at the loaded faces, generating a non-uniform, multiaxial stress state and increasing the apparent stiffness; the magnitude of this constraint grows with the ratio of constrained to free surface, which is known as the shape factor. An established empirical relation quantifies this dependence for quasistatic compression, formulated for cylindrical specimens under linear elasticity (Brown, 1996)

$$E_s = E(1 + \beta S^n), \tag{9}$$

where E_s is the effective compressive modulus of the tested sample (influenced by the shape of the sample), E is the compressive modulus of the tested material, $S = d/4L$ is the shape factor of the tested sample (assumed to be cylindrical) and β is a coefficient that captures the strength of boundary-condition–induced lateral constraint (typically $\beta \approx 2$ for cylindrical, nearly incompressible elastomers under bonded/high-friction interfaces), while n is the exponent that encodes the scaling with shape factor, commonly $n \approx 2$ reflecting a quadratic dependence (Brown, 1996; ISO 7743).

Conversely, the effect of the shape factor in the effective shear modulus obtained through torsion testing remains underexplored. Rheology standards for rotational rheometry of soft solids indicate that the optimal gap between plates (which corresponds to L) is between 0.5 mm and 3 mm (ISO 3219), while recent works prove that longer, rod-like samples, lead to better results (Borin et al., 2018). In fact, a recent work of the authors proposes an empirical model to address the effects of the shape factor in the determination of the quasistatic shear modulus of cylindrical samples (Cortazar-Noguerol et al., 2025):

$$G_s = G\frac{1 + \beta S^n}{1 + \alpha S^n}, \tag{10}$$

where G_s is the effective shear modulus of the tested sample, G is the shear modulus of the tested material, β, α and n are model parameters dependent on the material, being the values of β and n shared between Eqs. (9) and (10).

Combining Eqs. (2), (9) and (10), effective Poisson's ratio of the tested sample ν_s can be obtained in the quasistatic regime as

$$\nu_s = \frac{E}{2G}(1 + \alpha S^n) - 1 = \nu + \frac{E}{2G}\alpha S^n, \tag{11}$$

were

$$\nu = \frac{E}{2G} - 1 \tag{12}$$

represents Poisson's ratio of the tested material.

3. Materials and methods

This section describes the sample preparation process, the equipment used, and the experimental methods employed in this study.

3.1. Sample preparation

The material under study is a commercially available room-temperature vulcanizing (RTV) silicone rubber, ELASTOSIL® M 4644 A/B, produced by WACKER (ELASTOSIL® M 4644 A). This silicone rubber consists of two components: component A is the base material (PDMS + additives), and B is the curing agent. The mixture of these two components in a 10:1 wt ratio cures at room temperature in 24 h. Given the glassy transition temperature of the final product is ≤ -50 °C (Agirre-Olabide and Elejabarrieta, 2016), this material offers great stability at room temperature.

To be able to test a whole range of shape factors, different sample lengths L (3 and 10 mm) and diameters d (5, 10, 15 and 20 mm) are combined. This approach enables a systematic study of different geometries, as illustrated in Fig. 1, where the selected sample sizes are represented by square markers, ensuring an even distribution in terms of shape factor, visualized as a contour plot. Two different lengths and four different diameters are available, leading to 8 possible different shape factors from which 7 are selected to avoid overlapping. The resulting range of shape factors spans from 0.125 to 1.667.

To prepare this set of samples, two molds are designed and fabricated using polymethyl methacrylate (PMMA) sheets of 3 mm and 10 mm thicknesses. These molds are produced with a ROLAND MDX-40A (Modela MDX) 3D milling machine (Fig. 2 (a)). Each mold features cylindrical holes with diameters of 5, 10, 15, and 20 mm (Fig. 2 (b)).

During sample preparation, removing air bubbles from the material is essential, as their presence can influence the measured properties. To achieve this, component A is first placed inside a vacuum chamber (Fig. 2 (c)) and subjected to repeated vacuum cycles until all visible bubbles are eliminated. Once degassed, component B is introduced at a 10:1 (A:B) weight ratio, and the two components are thoroughly mixed using a glass rod. This mixing process inevitably reintroduces air bubbles, requiring additional vacuum cycles to minimize their presence.

Within 30 min of mixing, the degassed silicone rubber is carefully poured into the cylindrical molds. Further vacuum cycles are applied to ensure the material is free of bubbles before securing the mold's upper section with clamps. The samples are then left to cure for 24 h, after which the vulcanized specimens are demolded. For each nominal geometry, three individual samples are selected, resulting in a total of 21 samples, as shown in Fig. 2 (d).

3.2. Sample dimensions

The sample length and diameter are measured with a digital Vernier caliper with 0.01 mm resolution. To obtain the uncertainties in the preparation process, the mean value and standard deviation of the three samples for each nominal size is computed. The results are presented in Tables 1 and 2, where L_{nom} and d_{nom} represent the nominal length and

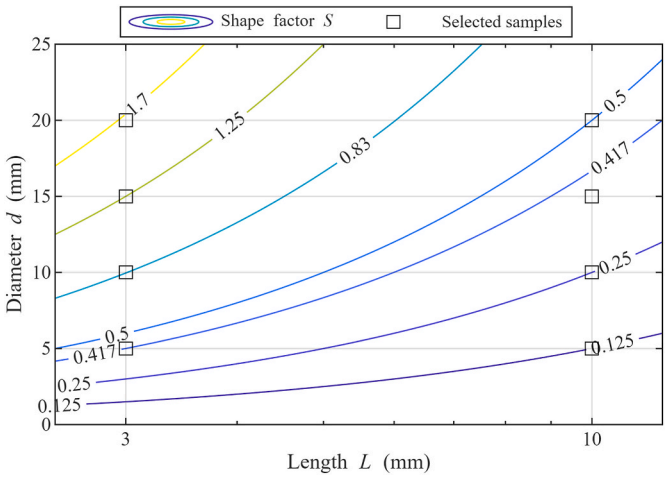

Fig. 1. Contour plot of constant shape factor lines as a function of sample diameter d and length L (logarithmic scale). The square markers indicate the sample sizes used in the experimental study.

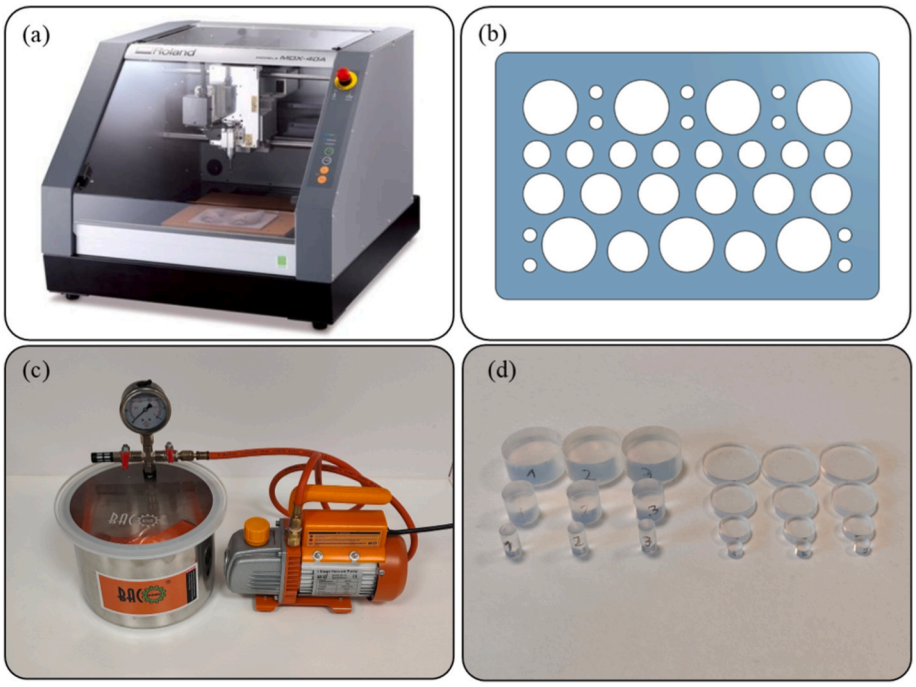

Fig. 2. Equipment and materials used for the preparation of silicone rubber samples: (a) ROLAND MDX-40A 3D milling machine; (b) 3D model of the molds; (c) vacuum chamber and pump and (d) 21 silicone rubber samples of various sizes tested throughout this work.

Table 1
Measurement results for the samples with nominal length $L_{nom} = 10$ mm.

$L_{nom} = 10$ mm			
d_{nom} (mm)	L (mm)	d (mm)	S
5	9.73 ± 0.02	5.00 ± 0.01	0.128 ± 0.001
10	9.76 ± 0.01	9.99 ± 0.01	0.256 ± 0.001
20	9.72 ± 0.03	20.00 ± 0.03	0.514 ± 0.002

Table 2
Measurement results for the samples with nominal length $L_{nom} = 3$ mm.

$L_{nom} = 3$ mm			
d_{nom} (mm)	L (mm)	d (mm)	S
5	3.01 ± 0.01	4.84 ± 0.01	0.402 ± 0.002
10	3.03 ± 0.01	9.81 ± 0.02	0.809 ± 0.004
15	3.00 ± 0.04	14.83 ± 0.03	1.24 ± 0.02
20	3.00 ± 0.01	19.80 ± 0.01	1.650 ± 0.005

diameter respectively.

Although the measured values do not exactly match the expected nominal dimensions, the deviation between samples with the same nominal dimensions falls below 1.5 % in every case.

3.3. Equipment

This subsection describes the experimental equipment used for the dynamic characterization of the prepared silicone rubber samples.

On the one hand, to measure the complex compressive modulus, a Dynamic Mechanical Analyzer (DMA) is used, specifically, the DMA Q800 model fabricated by T.A. Instruments (Fig. 3 (a)). The DMA is equipped with a compression clamp and can generate displacements up to 1 nm resolution applying force control within a range from 0.001 N to 18 N. Moreover, the theoretical frequency range of the equipment is from 0.1 Hz to 200 Hz, however, the upper limit heavily depends on the stiffness of the sample. Data acquisition is performed through Advantage for Q Series Version 2.9.2.396 software, provided by T.A. Instruments and the subsequent processing and analysis are carried out in MATLAB R2025a.

On the other hand, the complex shear modulus is determined using the Anton Paar Modular Compact Rheometer (MCR) 302e with a parallel plate configuration (Fig. 3 (b)). The rheometer can exert between 0.5 nN m and 230 mN m torque and 50 N maximum axial compressive force. It can measure angular displacements with a resolution of 0.05 μrad. The theoretical frequency range of the rheometer is between 16 nHz and 100 Hz, although the real application range, as in the DMA, depends also on the stiffness of the sample (Modular Compact Rheometer). Data acquisition is performed through RheoCompass v1.33.491, and the subsequent processing and analysis are carried out in MATLAB R2025a.

3.4. Experimental methods

With the aim of analyzing the influence of the sample shape factor on the effective complex moduli, dynamic compression and torsion tests were carried out on cylindrical specimens with different geometries. To correlate the complex compressive and shear moduli and compute the complex Poisson's ratio, compression and torsion tests were conducted under matched conditions—frequency, temperature, strain amplitude within the LVR, and axial pre-strain—and on the same specimens. These choices follow the spirit of Tschoegl's protocol (Tschoegl et al., 2002). Strict adherence to that protocol would require determining both moduli simultaneously on the same apparatus; in this study, the measurements were performed in separate tests and equipments with carefully matched conditions. The following subsection describes the experimental procedures employed to perform these tests and obtain the corresponding material properties.

Frequency-sweep experiments were conducted in the DMA (compression mode) and the rheometer (torsion mode) to obtain comparable datasets. The sweeps covered 0.1–10 Hz at discrete frequencies of 0.1, 0.2, 0.3, 0.6, 1.0, 1.5, 3.0, 5.0, and 10.0 Hz, and all tests were performed at room temperature (25 ± 2 °C). Because the silicone rubber lies in the viscoelastic rubbery regime, far from transition, small temperature variations within this range are not expected to affect the measured moduli.

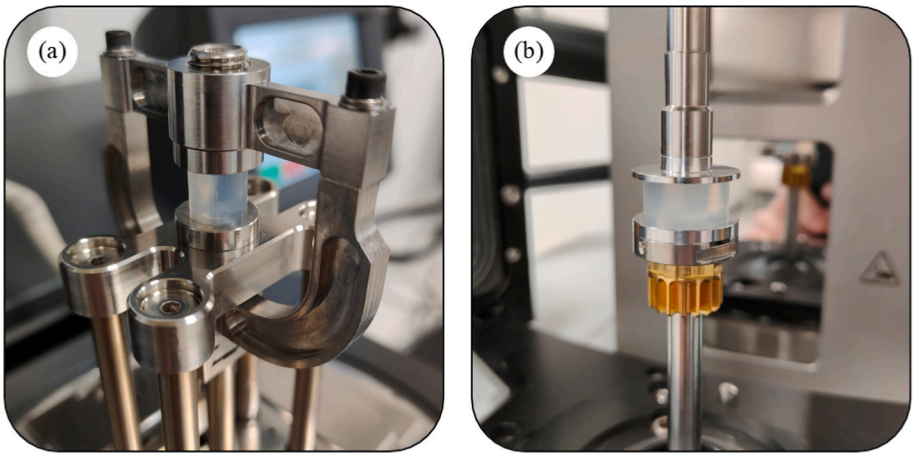

Fig. 3. Experimental equipment used for characterization: (a) dynamic mechanical analyzer (DMA) equipped with a compression clamp and (b) rheometer in a parallel plate configuration.

To ensure continuous contact in compression and no-slip in torsion a small axial pre-strain must be applied. The pre-strain was applied under force control (a constraint of this DMA equipment), with the force for each geometry computed from our previously established quasistatic relations between shape factor and the effective compressive modulus (Cortazar-Noguerol et al., 2025). Preliminary tests across multiple pre-strain levels confirmed that, while pre-strain can bias the measured moduli (Borin et al., 2018; Ayyildiz et al., 2015), this effect remained negligible within our operating window and no apparent slippage was detected in torsion tests. Consequently, an axial pre-strain of $\varepsilon_0 = 0.5$ % was adopted for both testing procedures.

Strain amplitudes were set from LVR tests in both compression (ISO 6721a) and torsion (Agirre-Olabide et al., 2014), leading to an amplitude of $\varepsilon = \gamma = 0.1$ % for both testing procedures. Because the torsional strain amplitude is diameter-dependent in torsion, the 'Plate diameter' parameter in RheoCompass was manually updated for each specimen to ensure that the imposed angular displacement generated the target shear strain for every geometry. The linear torsional response at these amplitudes further support absence of wall slip. Moreover, dry interfacial adhesion consistent with the Johnson-Kendall-Roberts contact mechanics (Ciavarella et al., 2019; Johnson et al., 1997) was qualitatively inferred from the measured negative normal force during parallel plate separation both in the DMA and rheometer equipment.

Repeatability was evaluated at two levels. Cross-sample repeatability was assessed by testing three independent specimens for each nominal size, and cross-test repeatability by performing three consecutive frequency sweeps per specimen under identical conditions. For each frequency, sweeps were averaged to obtain a specimen-level response, which was then averaged across the three specimens of the same nominal size to yield the reported moduli.

4. Experimental results

This section presents and discusses experimental results. The analysis is divided into three parts: the effective complex compressive modulus, the effective complex shear modulus, and the derivation of the effective complex Poisson's ratio. Each point corresponds to the mean of three consecutive frequency sweeps; the across-sweep standard deviation was <0.5 % for both procedures and is omitted. For clarity, only the mean across the three specimens of each nominal size is shown; between-specimen variability is discussed in the text.

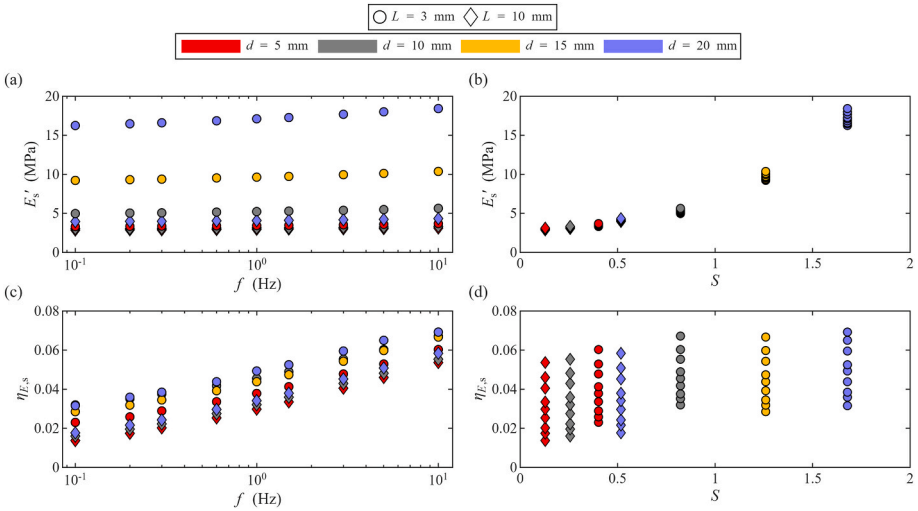

Fig. 4. Experimental results of the dynamic compressive tests. The length L is represented with different markers while the diameter d is represented by different colors: (a) effective storage modulus E_s' as a function of frequency f, (b) effective storage modulus E_s' as a function of shape factor S, (c) effective loss factor $\eta_{E,s}$ as a function of frequency f and (d) effective loss factor $\eta_{E,s}$ as a function of shape factor S.

4.1. Effective complex compressive modulus

Fig. 4 shows the experimental results of the effective complex compressive modulus of each nominal size in terms of its storage modulus and loss factor. The length is indicated by different markers while the diameter is indicated by different colors. Fig. 4 (a) and (b) show the dependence of the effective storage modulus on frequency and shape factor respectively and Fig. 4 (c) and (d) show the dependence of the effective loss factor on frequency and shape factor.

The effective storage modulus increases with frequency as shown in Fig. 4 (a) between a 9 % and a 14 % within the range tested, consistent with the expected viscoelastic behavior of the material in the rubbery region at room temperature (Agirre-Olabide and Elejabarrieta, 2016). The magnitude of this increase depends on the sample geometry, with lower shape factor samples showing a smaller rise than those with higher shape factors. Across specimens of identical nominal size, the standard deviation remained below 3 % over the entire frequency and geometry ranges.

Fig. 4 (c) indicates a stronger frequency dependence of the effective loss factor, with values increasing up to 300 % for low shape factor samples and 120 % for high shape factor ones. These results show that the sample's geometry affects not only the value of the effective complex compressive modulus but also its the frequency dependence. For a given nominal size, between-specimen standard deviation remained below 5 %.

Regarding the geometry effects, Fig. 4 (b) shows that the effective storage modulus increases monotonically with shape factor, reaching values more than four times greater in the highest shape factor samples. A slightly larger rise is observed at the highest frequency. In contrast, the effective loss factor shows a more moderate dependence on shape factor. As seen in Fig. 4 (d), it increases by approximately 130 % at 0.1 Hz and by only 30 % at 10 Hz. This suggests that the shape factor has a stronger effect on the energy storage component of the sample response than on the energy dissipation. However, the interplay between shape factor and frequency is more present in the effective loss factor variation.

In summary, the results demonstrate that both frequency and shape factor significantly influence the effective complex compressive modulus measured in dynamic compression tests, with a clear interdependence between their effects. Consequently, when developing a phenomenological model to extract the intrinsic material property, these variables cannot be treated as independent.

4.2. Complex shear modulus

The experimentally obtained effective complex shear modulus is shown in Fig. 5 in terms of its storage modulus and loss factor. The length of the samples is represented by different markers while the diameter is indicated by different colors. Fig. 5 (a) and (b) show the dependence of the effective shear storage modulus on frequency and shape factor respectively, and Fig. 5 (c) and (d) show the dependence of the effective loss factor on frequency and shape factor.

Existing work has examined inertial effects in rheometer measurements. Müller-Pavel et al. (Müller-Pabel et al., 2022) propose a criterion whereby data points with $\tau_{TOT}/\tau > 10$, where τ_{TOT} is the total shear-stress amplitude reported by the rheometer and τ is the shear stress borne by the specimen, show considerable inertial effects. Accordingly, in this work we follow the same criterion and data points that fulfill this condition are plotted as hollow symbols and excluded from subsequent analysis and curve fitting.

The effective storage modulus increases moderately with frequency (Fig. 5 (a)), consistent with the rubbery viscoelastic behavior of the material under shear loading at room temperature. The extent of this increase depends on shape factor, with both low and high shape factor samples showing similar trends, although the increase is slightly greater for the latter. The standard deviation between samples of the same nominal size remained below 3 %.

Fig. 5 (c) shows a more pronounced frequency dependence on the effective loss factor, with increases of roughly 200 % observed across the full range of shape factors. These results confirm that the dynamic shear response of the samples exhibits a frequency dependence that is modulated by geometry, although to a lesser extent than the dynamic compressive response. For each nominal size, inter-specimen standard deviation remained under 6 %.

The influence of shape factor is further clarified in Fig. 5 (b) and (d). The effective storage modulus decreases with an increasing shape factor by approximately 15 % in the range tested. In contrast, the effective loss factor increases with shape factor, approximately 45 % at the lowest frequency and 15 % at the highest. These trends indicate that the shape factor influences not only the magnitude of the effective complex shear modulus but also its frequency dependence, being the lower frequencies the most affected ones.

Finally, consistent with the results obtained for the effective complex compressive modulus, the effective complex shear modulus is also governed by the combined effects of frequency and specimen geometry. Hence, models developed to identify the intrinsic material behavior

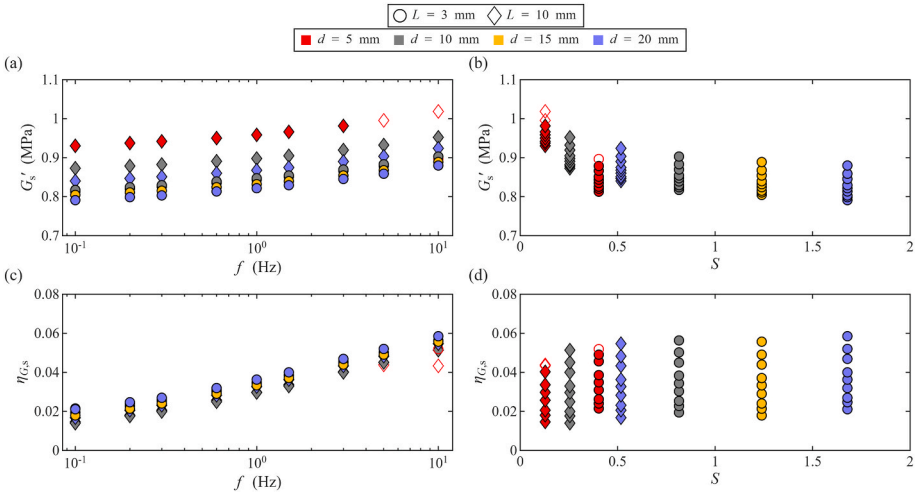

Fig. 5. Experimental results of the dynamic torsion tests. The length of the sample L is represented with different markers while the diameter d is represented by different colors: (a) storage modulus G_s' as a function of frequency f, (b) storage modulus G_s' as a function of shape factor S, (c) loss factor $\eta_{G,s}$ as a function of frequency f and (d) loss factor $\eta_{G,s}$ as a function of shape factor S. Hollow markers represent the points where the inertial effects of the rheometer are significant.

from these measurements should account for their mutual dependence.

4.3. Effective complex Poisson's ratio

From the experimentally determined effective complex compressive and shear moduli of each sample, effective complex Poisson's ratio can be determined using Eq. (2). Fig. 6 shows the results obtained for the effective complex Poisson's ratio of each sample. The length of the samples is represented by different markers while the diameter is indicated by different colors.

Fig. 6 (a) and (c) show the frequency dependence of the effective complex Poisson's ratio. The real part shows a mild increase across all the samples, this increase being greater in the highest shape factor samples. The loss factor exhibits only minor variations across the tested frequency range, and its frequency dependence does not show a systematic correlation with the shape factor. While the standard deviation between samples of the same nominal size remains under 6 % for the real part, the deviation in the loss factor is greater. For the lowest shape factor the standard deviation reaches 250 % and the rest of the shape factors show a standard deviation between 15 % and 50 %. This significative deviations can be explained by the fact that the loss factor is very close to zero, which leads to considerable relative errors.

The influence of shape factor is more pronounced, as shown in Fig. 6 (b) and (d). The real part increases steeply with the shape factor, reaching values well above the theoretical upper bound of 0.5 for incompressible isotropic materials. This highlights the substantial geometric distortion introduced into the effective viscoelastic response. Although the effect of the shape factor on the loss factor is less pronounced, all samples with $S > 0.125$ exhibit negative values. Since the loss factor of the complex Poisson's ratio cannot be negative for isotropic homogeneous materials (Tschoegl et al., 2002; Pritz, 1998, 2000), this result indicates that the effective values lose physical representativeness under these geometric conditions and must be corrected to account for the shape factor of the samples.

5. Modelling and analysis

The experimental results reflect the effective dynamic response of the tested samples, which is influenced by their own sample geometry. To recover the intrinsic material frequency response, a phenomenological model is proposed that accounts for shape factor effects in both compression and shear in the analyzed frequency range. This model enables the identification of frequency-dependent material moduli, which are then used to reconstruct the complex Poisson's ratio.

This section presents a frequency-dependent model to correct shape factor effects in compressive and torsion tests. First, the effect of shape factor and frequency is modeled using analytical expressions. Next, these parameters are identified by simultaneous curve-fitting of compressive and shear data. Then, the fitted parameters are analyzed to evaluate the frequency dependence of the intrinsic moduli and shape correction terms. Finally, the complex Poisson's ratio is reconstructed from the corrected moduli, and its frequency dependence is described.

5.1. Model proposal

Based on the results shown in Section 4.3, it is assumed that the effect of the shape factor and frequency are coupled, therefore, the parameters of the proposed model must be frequency dependent. Considering this assumption and based on the model proposed in our previous work (Cortazar-Noguerol et al., 2025), the effect of the shape factor and frequency on the dynamic properties of the material can be described by

$$E_s^*(f,S) = E^*(f)\left[1+\beta^*(f)S^{n(f)}\right], \tag{13}$$

$$G_s^*(f,S) = G^*(f)\frac{1+\beta^*(f)S^{n(f)}}{1+\alpha^*(f)S^{n(f)}}, \tag{14}$$

and

$$\nu_s^*(f,S) = \nu^*(f) + \frac{E^*(f)}{2G^*(f)}\alpha^*(f)S^{n(f)}, \tag{15}$$

where $E^* = E'(1+i\eta_E)$ is the complex compressive modulus of the material, $G^* = G'(1+i\eta_G)$ is the complex shear modulus of the material, $\nu^* = \nu'(1+i\eta_\nu)$ is the complex Poisson's ratio of the material, and $\beta^* = \beta' + i\beta''$ and $\alpha^* = \alpha' + i\alpha''$ are complex and frequency dependent parameters of the model. Given there is no oscillatory component in the effective properties of the samples, n must be real but, in principle, can depend on the frequency. This leads to a model with 4 complex and 1 real frequency dependent parameters.

5.2. Parameter identification by curve-fitting

To obtain the value of the five frequency dependent parameters, the function '*fmincon*' of MATLAB R2025a is used. The estimation problem is formulated as a nonlinear constrained minimization and solved with the interior-point algorithm, which enforces bounds and via a barrier

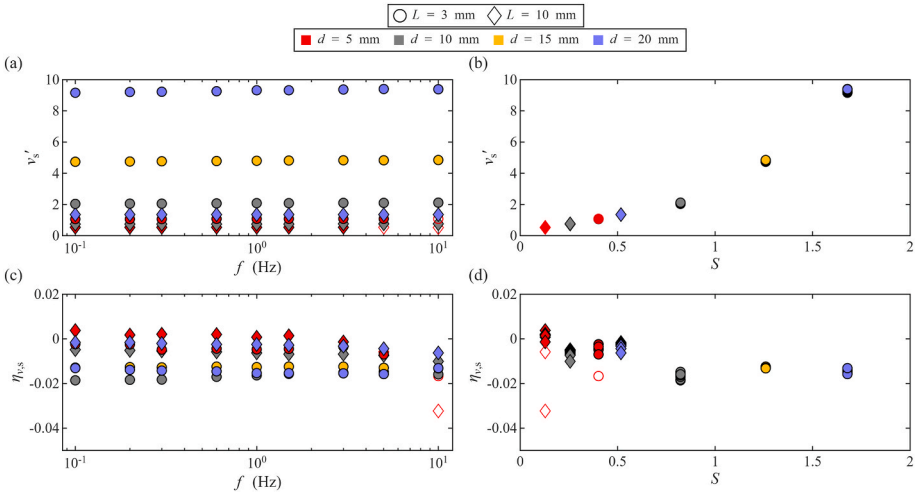

Fig. 6. Effective complex Poisson's ratio results, obtained from the effective complex compressive and shear moduli of each sample. The length of the sample L is represented with different markers while the diameter d is represented by different colors. (a) Real part of complex Poisson's ratio ν_s' as a function of frequency f and (b) as a function of shape factor S; (c) loss factor of complex Poisson's ratio $\eta_{\nu,s}$ as a function of frequency f and (d) as a function of shape factor S.

formulation and computes search directions by approximately solving the Karush–Kuhn–Tucker system with quasi-Newton Hessian updates and a line-search globalization strategy (Mathworks fmincon documentation). High limits on function evaluations and iterations were set to avoid premature termination, and strict tolerances on objective reduction and step norm were imposed to prevent convergence to flat or ill-conditioned regions. This configuration increases computational cost but yields reproducible curve-fitting results.

Given the '*fmincon*' function is limited to real parameters, the real and imaginary parts of every parameter need to be treated separately. Moreover, each parameter takes a value for each frequency, leading to a total of 81 different parameter values in the curve fitting process. Given $E_s^*(f,S)$ and $G_s^*(f,S)$ as defined by Eqs. (13) and (14) share the parameters β^* and n, the curve-fitting of both the compressive and shear results is done simultaneously, leading to the following objective function:

$$g(\mathbf{X}) = g_1(\mathbf{X}) + g_2(\mathbf{X}) + g_3(\mathbf{X}) + g_4(\mathbf{X}), \tag{16}$$

with

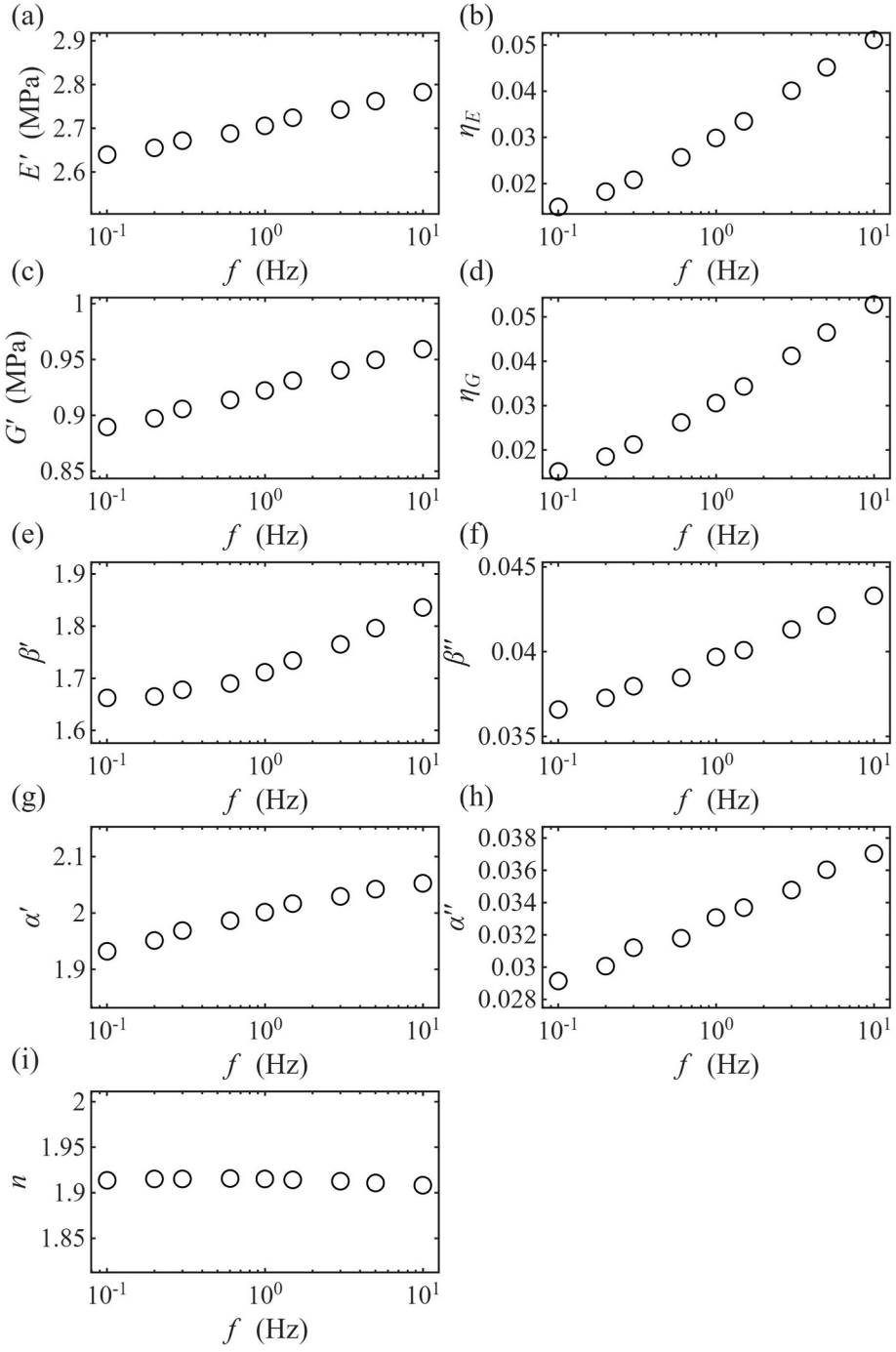

Fig. 7. Experimental results and fitted curves of the sample dynamic moduli and Poisson's ratio as a function of shape factor S for different frequencies. The frequency f of each measurement is represented by a different marker and color: (a) compressive storage modulus E_s', (b) compressive loss factor $\eta_{E,s}$ (c) shear storage modulus G_s', (d) shear loss factor $\eta_{G,s}$, (e) Poisson's ratio's real part ν_s', and (f) Poisson's ratio's loss factor $\eta_{\nu,s}$. Experimental data points are shown as markers and model predictions are shown as continuous lines. Hollow markers indicate measurements excluded from the fit due to inertial effects in the torsion tests.

$$g_1(\mathbf{X}) = \sum_{i,j} \left\{ \left[\frac{E'_{s,i,j} - E'_s\left(\mathbf{X}\left(f_j\right), S_i\right)}{\max_j\left(E'_{s,i,j}\right)} \right]^2 + \left[\frac{\eta_{E,s,i,j} - \eta_{E,s}\left(\mathbf{X}\left(f_j\right), S_i\right)}{\max_j\left(\eta_{E,s,i,j}\right)} \right]^2 \right\}, \tag{17}$$

$$g_2(\mathbf{X}) = \sum_{i,j} \left\{ \left[\frac{G'_{s,i,j} - G'_s\left(\mathbf{X}\left(f_j\right), S_i\right)}{\max_j\left(G'_{s,i,j}\right)} \right]^2 + \left[\frac{\eta_{G,s,i,j} - \eta_{G,s}\left(\mathbf{X}\left(f_j\right), S_i\right)}{\max_j\left(\eta_{G,s,i,j}\right)} \right]^2 \right\}, \tag{18}$$

$$g_3(\mathbf{X}) = \sum_{j} \left\{ \frac{1}{0.5} \left[\frac{\eta_v\left(f_j\right)}{\eta_G\left(f_j\right)} - 1 + 2\nu'\left(f_j\right) \right] \right\}^2, \tag{19}$$

and

$$g_4(\mathbf{X}) = \sum_{x \in \mathbf{X}} \mathrm{std}\left(\frac{\partial^2 x}{\partial f^2} \right) \tag{20}$$

where g is the non-linear objective function, g_1 and g_2 compare the predicted and the experimental effective storage modulus and loss factors, g_3 introduces the approximation done by Pritz, shown in Eq. (8) and g_4 imposes regularization by penalizing the standard deviation of the second-order frequency derivative of each parameter $x \in \mathbf{X}$, thereby enforcing smoothness across frequencies (Gu, 2008). $\mathbf{X}\left(f_j\right) = \left\{ E^*\left(f_j\right), G^*\left(f_j\right), \beta^*\left(f_j\right), \alpha^*\left(f_j\right), n\left(f_j\right) \right\}$ is the set of parameter values to be identified. The terms $E'_{s,i,j}$ and $G'_{s,i,j}$ denote the experimental effective compressive and shear storage moduli for the shape factor S_i and frequency f_j, respectively, while $\eta_{E,s,i,j}$ and $\eta_{G,s,i,j}$ are the corresponding experimental effective loss factors. The functions $E'_s(\mathbf{X}, S, f)$ and $G'_s(\mathbf{X}, S, f)$ represent the model predicted effective complex compressive and shear moduli, obtained from Eqs. (13) and (14) respectively. Each term of functions g_1 and g_2 is normalized by the maximum value across the whole frequency range for each shape factor (represented by the function $\max_j()$). The terms in function g_3 are normalized by the maximum expected value of the complex Poisson's ratio's real part, i.e. 0.5. All in all, this cost function formulation ensures that the fitted parameters accurately reconstruct the experimental data (terms g_1 and g_2), preserve physical plausibility (term g_3) and evolve smoothly with frequency (term g_4).

5.3. Model results and analysis

For model validation, Fig. 7 compares the measured shape-factor dependence with the model predictions across all test frequencies. Symbols denote experimental values of the effective moduli and complex Poisson's ratio; solid curves show the model evaluated with fitted, frequency-specific parameters. Data excluded from fitting are plotted as hollow symbols.

Model–data correspondence is consistent across the explored shape-factor and frequency ranges. The model reproduces the shape factor dependence at each frequency and remains within experimental dispersion for the effective moduli and complex Poisson's ratio. Residuals are smallest at intermediate shape factors and remain bounded toward the extremes, with the largest deviations at the highest frequency and lowest shape factor, where the excluded points already indicate reduced data reliability.

Fig. 8 shows the fitted parameter values at each frequency. Panels (a–d) display the material's intrinsic viscoelastic properties, E^* and G^* (including their storage modulus and loss factor), which will be analyzed in the next section and are shown here only for completeness. Panels (e–h) show β', β'', α' and α'',each varying smoothly and monotonically increasing with frequency. Panel (i) shows the exponent n, which remains effectively constant across 0.1–10 Hz ($n \approx 1.9$) with minimal variation.

In the low-frequency limit, the fitted parameters approach the previously reported quasi-static values (Cortazar-Noguerol et al., 2025): $\beta' \approx 1.7$, $\alpha' \approx 2$, and $n \approx 1.9$. This confirms that the dynamic fit reduces to the known static case as $f \to 0$. Away from this limit, the frequency dependence of β^* and α^* shows that geometry correction must be expressed as a function of frequency. In contrast, the exponent n remains

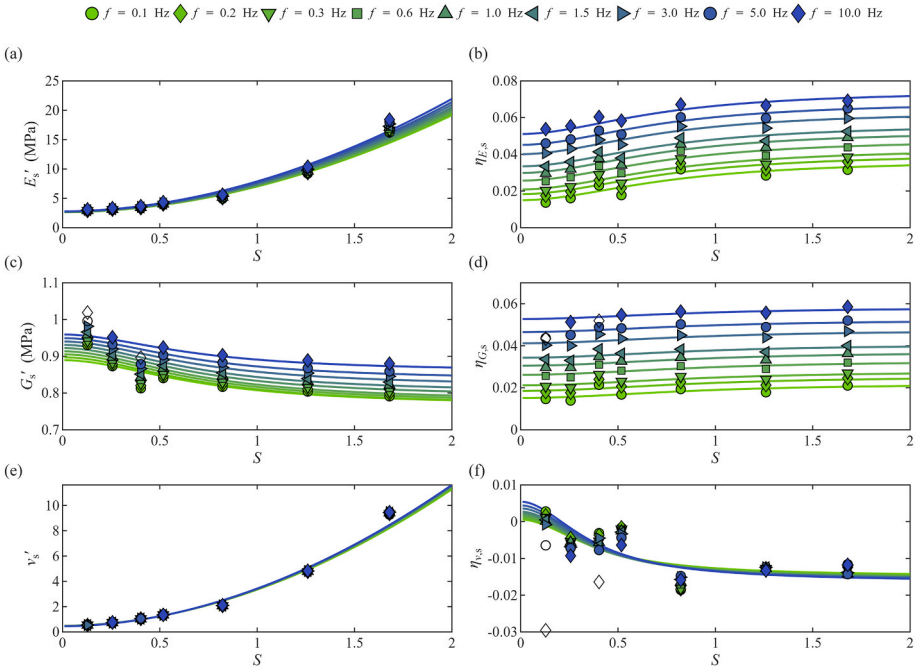

Fig. 8. Frequency dependence of the fitted model parameters obtained from the curve fitting procedure: (a) real part of the material's compressive modulus E', (b) loss factor of the material's compressive modulus η_E, (c) real part of the material's shear modulus G', (d) loss factor of the material's shear modulus η_G, (e) real part of β^*, (f) imaginary part of β^*, (g) real part of α^*, (h) imaginary part of α^*, and (i) shape factor exponent n.

approximately constant across the measured frequency range.

5.4. Material's dynamic properties

This subsection presents the material's intrinsic dynamic mechanical properties obtained by fitting proposed model to the obtained experimental data. The complex compressive E^* and shear G^* moduli are obtained as model parameters from Eqs. (13) and (14) respectively while the complex Poisson's ratio is computed from

$$\nu^* = \frac{E^*}{2G^*} - 1. \tag{21}$$

To obtain an error estimation of these properties, the relative root mean square error (RRMSE) has been computed for each magnitude comparing the model predictions and the experimental data (see Fig. 8):

$$\mathrm{RRMSE}_y(f) = \sqrt{\frac{1}{N_S}\sum_{k=1}^{N_S}\left(\frac{\widehat{y}(S_k,f) - y(S_k,f)}{y(S_k,f)}\right)^2}, y \in \{E', \eta_E, G', \eta_G, \nu', \eta_\nu\}, \tag{22}$$

where $y(S_k,f)$ is the experimental value at (S_k,f) and $\widehat{y}(S_k,f)$ is the corresponding model prediction. N_S is the total number of shape factors considered.

Fig. 9 shows the material's dynamic mechanical properties extracted from the developed model. Panels (a–d) plot E^* and G^* and panels (e–f) plot ν^* computed from Eq. (21). Circles are the magnitude estimates, and error bars are the RRMSE at each frequency as defined in Eq. (22), evaluated over the full set of shape factors.

The complex moduli show the expected viscoelastic response of silicone rubber in the rubbery region (Agirre-Olabide and Elejabarrieta, 2016). The compressive storage modulus E' increases from 2.65 to 2.80 MPa while its loss factor η_E shows a greater increase, from 0.01 to 0.05 approximately. Regarding the shear modulus, its storage modulus G' varies between 0.89 and 0.95 MPa and its loss factor η_G increases between 0.01 and 0.05. In both cases, the computed RRMSE stays within acceptable limits.

The complex Poisson's ratio shows weaker frequency dependence. Its real part ν' remains almost constant but with a subtle monotonical decrease from 0.48 in the lowest frequency to 0.46 in the highest. These values are consistent with the observed Poisson's ratio in the quasistatic case ($\nu = 0.48$) for this same material (Cortazar-Noguerol et al., 2025). The loss factor η_ν shows a positive increasing trend with frequency, but with excessive errors to draw strong conclusions.

Concluding, the behavior shown by the material's complex moduli is the expected for a silicone rubber in the viscoelastic rubbery region. In addition, Poisson's ratio's behavior is the typical for an isotropic homogeneous nearly incompressible material, with a decreasing real part and an increasing, positive loss factor (Tschoegl et al., 2002; Pritz, 1998, 2000). This procedure however is only valid for homogeneous nearly incompressible materials given the term g_3 defined in Eq. (19) only stands under this assumption.

6. Conclusions

This work has investigated the influence of sample shape factor on the dynamic characterization of viscoelastic properties, with a focus on the complex compressive and shear moduli and the complex Poisson's ratio. Compression and torsion tests have been performed on cylindrical silicone rubber samples with varying geometries and over a frequency range from 0.1 to 10 Hz. The measured effective moduli have exhibited a clear dependence on both shape factor and frequency, demonstrating

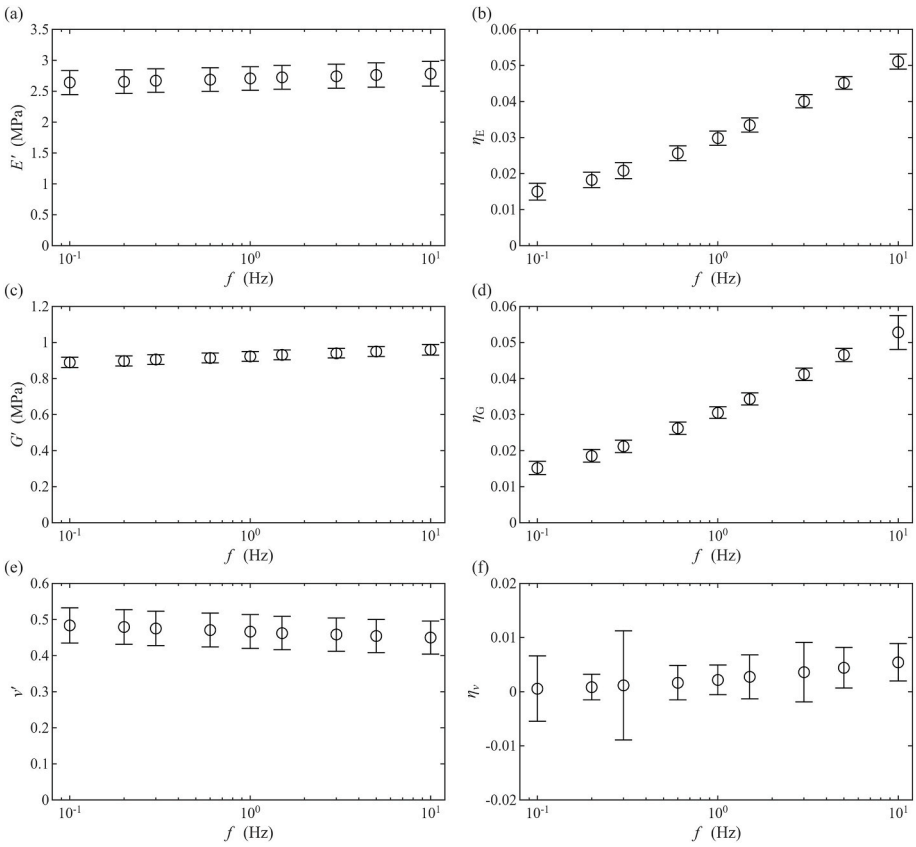

Fig. 9. Material's intrinsic dynamic mechanical properties extracted from the shape-factor dependent model: (a) storage modulus of the complex compressive modulus E', (b) loss factor of the complex compressive modulus η_E, (c) storage modulus of the complex shear modulus G', (d) loss factor of the complex shear modulus η_G, (e) real part of the complex Poisson's ratio ν' and (f) loss factor of the complex Poisson's ratio η_ν.

that these effects are coupled and not independently separable.

A phenomenological correction model has been developed to obtain the dynamic properties of the material, extending a previous model for the quasistatic case. The model introduces frequency-dependent parameters to describe the geometry-induced deviations in the measured compressive and shear moduli. The model has been fitted to data from seven sample geometries assuming the material is nearly incompressible. This has allowed the extraction of geometry-independent complex moduli that vary smoothly with frequency and accurately represent both the storage and loss components of the material response.

The material's complex Poisson's ratio has been determined with the corrected complex moduli. The real component has been observed to decrease slightly with increasing frequency, falling from approximately 0.48 at the lowest frequency to about 0.46 at the highest. These values align with independent quasistatic measurements on the same material. The corresponding loss factor remains positive and rises from 0.001 to 0.004 over the same frequency range. Taken together, the subtle frequency sensitivity of the real part and the monotonic increase of the loss factor represent the expected response for an isotropic, homogeneous nearly incompressible material.

CRediT authorship contribution statement

Julen Cortazar-Noguerol: Writing – original draft, Visualization, Validation, Software, Methodology, Investigation, Formal analysis, Data curation, Conceptualization. **Fernando Cortés:** Writing – review & editing, Supervision, Methodology, Investigation, Formal analysis, Conceptualization. **María Jesús Elejabarrieta:** Writing – review & editing, Supervision, Project administration, Funding acquisition, Formal analysis, Conceptualization.

Declaration of generative ai and ai-assisted technologies in the Writing process

During the preparation of this work the authors used ChatGPT-4 to improve the readability and language of the manuscript. After using this tool, the authors reviewed and edited the content as needed and take full responsibility for the content of the published article.

Declaration of competing interest

The authors declare that they have no known competing financial interests or personal relationships that could have appeared to influence the work reported in this paper.

Acknowledgements

This research has been supported by the University of Deusto Research Training Grants Program (grant reference number FPI UD_2023_07) and the Department of Education for the Research Group program IT1507-22.

APPENDIX A. ADDITIONAL MATHEMATICAL EXPRESSIONS

This appendix presents explicit expressions for the storage modulus, loss modulus, and loss factor of the effective compressive and shear moduli and the effective Poisson's ratio.

First, the effective compressive modulus can be written in terms of its storage modulus, loss modulus and loss factor as:

$$E_s' = E'[1 + (\beta' - \eta_E \beta'')S^n], \tag{A.1}$$

$$E_s'' = E'\eta_E[1 + (\beta' + \beta''/\eta_E)S^n], \tag{A.2}$$

and

$$\eta_{E,s} = \eta_E \frac{1 + (\beta' + \beta''/\eta_E)S^n}{1 + (\beta' - \eta_E\beta_E'')S^n}, \tag{A.3}$$

respectively.

Next, the effective shear modulus can be written in terms of its storage modulus loss modulus and loss factor as:

$$G_s' = \frac{G'\{1 + [\beta' + \alpha' + \beta'\alpha' + \beta''\alpha'' - \eta_G(\beta'' - \alpha'' - \beta'\alpha'' + \beta''\alpha')]S^n\}}{(1 + \alpha' S^n)^2 + (\alpha'' S^n)^2}, \tag{A.4}$$

$$G_s'' = \frac{G'\eta_G\{1 + [\beta' + \alpha' + \beta'\alpha' + \beta''\alpha'' + (\beta'' - \alpha'' - \beta'\alpha'' + \beta''\alpha')/\eta_G]S^n\}}{(1 + \alpha' S^n)^2 + (\alpha'' S^n)^2}, \tag{A.5}$$

and

$$\eta_{G,s} = \eta_G \frac{1 + [\beta' + \alpha' + \beta'\alpha' + \beta''\alpha'' + (\beta'' - \alpha'' - \beta'\alpha'' + \beta''\alpha')/\eta_G]S^n}{1 + [\beta' + \alpha' + \beta'\alpha' + \beta''\alpha'' - \eta_G(\beta'' - \alpha'' - \beta'\alpha'' + \beta''\alpha')]S^n}, \tag{A.6}$$

respectively.

Finally, the effective Poisson's ratio can be written in terms of its storage modulus loss modulus and loss factor as:

$$\nu_s' = \nu' + \frac{E'S^n[\alpha'(1 + \eta_E\eta_G) - \alpha''(\eta_E - \eta_G)]}{2G'(1 + \eta_G{}^2)}, \tag{A.7}$$

$$\nu_s'' = \nu'\eta_\nu + \frac{E'S^n[\alpha''(1 + \eta_E\eta_G) + \alpha'(\eta_E - \eta_G)]}{2G'(1 + \eta_G{}^2)}, \tag{A.8}$$

and

$$\eta_{\nu,s} = \frac{\eta_{\nu} + \frac{E'S^n[\alpha''(1+\eta_E\eta_G)+\alpha'(\eta_E-\eta_G)]}{2\nu' G'(1+{\eta_G}^2)}}{1 + \frac{E'S^n[\alpha'(1+\eta_E\eta_G)-\alpha''(\eta_E-\eta_G)]}{2\nu' G'(1+{\eta_G}^2)}}, \tag{A.9}$$

respectively.

Data availability

Data will be made available on request.

References

Adrover-Monserrat, B., García-Vilana, S., Sánchez-Molina, D., Llumà, J., Jerez-Mesa, R., Travieso-Rodriguez, J.A., 2022. Viscoelastic characterization of a thermoplastic elastomer processed through material extrusion. Polymers 14, 2914. https://doi.org/10.3390/polym14142914.

Agirre-Olabide, I., Elejabarrieta, M.J., 2016. Maximum attenuation variability of isotropic magnetosensitive elastomers. Polym. Test. 54, 104–113. https://doi.org/10.1016/j.polymertesting.2016.06.021.

Agirre-Olabide, I., Berasategui, J., Elejabarrieta, M.J., Bou-Ali, M.M., 2014. Characterization of the linear viscoelastic region of magnetorheological elastomers. J. Intell. Mater. Syst. Struct. 25, 2074–2081. https://doi.org/10.1177/1045389X13517310.

Ahmed, K., 2009. The torsional rheometer: a new testing method for assessing rheological properties of elastomers and hydrocolloids. https://doi.org/10.13140/RG.2.1.4137.2569.

Alam, M.N., 2024. Advances in functional rubber and elastomer composites. Polymers 16, 1726. https://doi.org/10.3390/polym16121726.

Alarifi, I.M., 2023. A comprehensive review on advancements of elastomers for engineering applications. Advanced Industrial and Engineering Polymer Research 6, 451–464. https://doi.org/10.1016/j.aiepr.2023.05.001.

Annarasa, V., Popov, A.A., De Focatiis, D.S.A., 2020. A phenomenological constitutive model for the viscoelastic deformation of elastomers. Mech. Time-Dependent Mater. 24, 463–479. https://doi.org/10.1007/s11043-020-09452-2.

Asp, M., Jutzeler, E., Kochanowski, J., Kerr, K., Song, D., Gupta, S., Carroll, B., Patteson, A., 2022. A torsion-based rheometer for measuring viscoelastic material properties. The Biophysicist 3, 94–105. https://doi.org/10.35459/tbp.2020.000172.

Ayyildiz, M., Cinoglu, S., Basdogan, C., 2015. Effect of normal compression on the shear modulus of soft tissue in rheological measurements. J. Mech. Behav. Biomed. Mater. 49, 235–243. https://doi.org/10.1016/j.jmbbm.2015.05.011.

Bodin, J.N., Shen, K., Zeng, S., Sun, L., 2024. Expanding horizons: diverse applications of rubbers and elastomers in emerging technologies. Rubber Chem. Technol. 97, 93–117. https://doi.org/10.5254/rct-d-23-00034.

Boiko, A.V., Kulik, V.M., Seoudi, B.M., Chun, H.H., Lee, I., 2010. Measurement method of complex viscoelastic material properties. Int. J. Solid Struct. 47, 374–382. https://doi.org/10.1016/j.ijsolstr.2009.09.037.

Borin, D., Kolsch, N., Stepanov, G., Odenbach, S., 2018. On the oscillating shear rheometry of magnetorheological elastomers. Rheol. Acta 57, 217–227. https://doi.org/10.1007/s00397-018-1071-2.

Bower, A.F., 2010. Applied Mechanics of Solids. CRC Press, Boca Raton, Fla.

Brown, R.P., 1996. Physical Testing of Rubber. Springer Netherlands, Dordrecht. https://doi.org/10.1007/978-94-011-0529-3.

Chakraborti, S., Banerjee, P.S., Basu, D., Wießner, S., Heinrich, G., Das, A., Banerjee, S.S., 2025. Elastomers for soft electronics: a review from the material's perspective. Adv. Eng. Mater. 27. https://doi.org/10.1002/adem.202402458.

Ciavarella, M., Joe, J., Papangelo, A., Barber, J.R., 2019. The role of adhesion in contact mechanics. J. R. Soc., Interface 16, 20180738. https://doi.org/10.1098/rsif.2018.0738.

Cortazar-Noguerol, J., Cortés, F., Sarría, I., Elejabarrieta, M.J., 2024. Preload influence on the dynamic properties of a polyurethane elastomeric foam. Polymers 16, 1844. https://doi.org/10.3390/polym16131844.

Cortazar-Noguerol, J., Cortés, F., Agirre-Olabide, I., Elejabarrieta, M.J., 2025. Compression and torsion testing for elastic moduli and Poisson's ratio characterization in silicone rubber samples with varying shape factors. Polym. Test., 108858 https://doi.org/10.1016/j.polymertesting.2025.108858.

Dessi, C., Coppola, S., Vlassopoulos, D., 2021. Dynamic mechanical analysis with torsional rectangular geometry: a critical assessment of constrained warping models. J. Rheol. 65, 325–335. https://doi.org/10.1122/8.0000207.

Dynamic mechanical analysis (DMA). In: Thermal Analysis of Polymers, first ed., 2009. Wiley, pp. 387–495. https://doi.org/10.1002/9780470423837.ch5.

Edwards, S.F., Takano, H., Terentjev, E.M., 2000. Dynamic mechanical response of polymer networks. J. Chem. Phys. 113, 5531–5538. https://doi.org/10.1063/1.1290134.

Ehrig, T., Modler, N., Kostka, P., 2018. Compression and frequency dependence of the viscoelastic shear properties of flexible open-cell foams. Polym. Test. 70, 151–161. https://doi.org/10.1016/j.polymertesting.2018.06.036.

ELASTOSIL® M 4644 A/B | Room Temperature Curing Silicone Rubber (RTV-2) | Wacker Chemie AG, WACKER Website (n.d.). https://www.wacker.com/h/en-us/c/elastosil-m-4644-ab/p/000005351 (accessed February 6, 2025).

Esmaeeli, R., Aliniagerdroudbari, H., Hashemi, S.R., Jbr, C., Farhad, S., 2019. Designing a new dynamic mechanical analysis (DMA) system for testing viscoelastic materials at high frequencies. Model. Simulat. Eng. 2019, 1–9. https://doi.org/10.1155/2019/7026267.

Fauser, D., Rodríguez Agudo, J.A., Madadi, H., Haeberle, J., Renner, J., Steeb, H., 2025. Complex Poisson's ratio for viscoelastic materials: direct and indirect measurement methods and their correlation. Proc. R. Soc. A A. 481. https://doi.org/10.1098/rspa.2024.0543.

Gordaninejad, F., Wang, X., Mysore, P., 2012. Behavior of thick magnetorheological elastomers. J. Intell. Mater. Syst. Struct. 23, 1033–1039. https://doi.org/10.1177/1045389X12448286.

Gu, C., 2008. Smoothing noisy data via regularization: statistical perspectives. Inverse Probl. 24, 034002. https://doi.org/10.1088/0266-5611/24/3/034002.

Hancox, N.L., 1972. The use of a torsion machine to measure the shear strength and modulus of unidirectional carbon fibre reinforced plastic composites. J. Mater. Sci. 7, 1030–1036. https://doi.org/10.1007/bf00550067.

Henriques, I.R., Borges, L.A., Costa, M.F., Soares, B.G., Castello, D.A., 2018. Comparisons of complex modulus provided by different DMA. Polym. Test. 72, 394–406. https://doi.org/10.1016/j.polymertesting.2018.10.034.

Hilton, H.H., Yi, S., 1998. The significance of (an)isotropic viscoelastic poisson ratio stress and time dependencies. Int. J. Solid Struct. 35, 3081–3095. https://doi.org/10.1016/s0020-7683(97)00357-0.

Inman, D.J., 2014. Engineering Vibration, fourth ed., International edition. Pearson Education Limited, Harlow, Essex.

ISO 3219-2:2022 Rheology - Part 2: General Principles of Rotational and Oscillatory Rheometry, ISO, n.d. https://www.une.org/encuentra-tu-norma/busca-tu-norma/norma?c=N0068730 (accessed January 28, 2025).

ISO 6721-12:2022 Plastics - Determination of Dynamic Mechanical Properties - Part 12: Compressive Vibration - Non-Resonance Method, ISO, n.d. https://www.iso.org/standard/81831.html.

ISO 6721-10:2015 Plastics - Determination of Dynamic Mechanical Properties - Part 10: Complex Shear Viscosity Using a parallel-plate Oscillatory Rheometer, ISO, n.d. https://www.iso.org/standard/62159.html.

ISO 6721-7:2019 | normas AENOR, (n.d.). https://tienda.aenor.com/norma-iso-6721-7-2019-073147 (accessed May 14, 2025).

ISO 7743:2017 Rubber, Vulcanized or Thermoplastic — Determination of Compression stress-strain Properties, ISO, n.d. https://www.iso.org/standard/72784.html (accessed January 28, 2025).

Johnson, K.L., Kendall, K., Roberts, A.D., 1997. Surface energy and the contact of elastic solids. Proceedings of the Royal Society of London. A. Mathematical and Physical Sciences 324, 301–313. https://doi.org/10.1098/rspa.1971.0141.

Jones, D.I.G., 2001. Handbook of Viscoelastic Vibration Damping. J. Wiley, Chichester ; New York.

Jutzeler, E., Asp, M., Kerr, K., Song, D., Patteson, A., 2020. A torsion-based rheometer for measuring viscoelastic material properties. https://doi.org/10.1101/2020.09.16.288415.

Lakes, R.S., Wineman, A., 2006. On poisson's ratio in linearly viscoelastic solids. J. Elasticity 85, 45–63. https://doi.org/10.1007/s10659-006-9070-4.

Li, R., Sun, L.Z., 2011. Dynamic mechanical analysis of silicone rubber reinforced with multi-walled carbon nanotubes. Interact. Multiscale Mech. 4, 239–245. https://doi.org/10.12989/IMM.2011.4.3.239.

Liu, X., Liu, C., Zhu, D., Lin, J., 2023a. A visco-hyperelastic constitutive model to characterize the stress-softening behavior of ethylene propylene diene monomer rubber. Polymers 15, 3388. https://doi.org/10.3390/polym15163388.

Liu, X., Zhu, D., Lin, J., Zhang, Y., 2023b. Temperature and frequency dependence of the dynamic viscoelastic properties of silicone rubber. Polymers 15, 3005. https://doi.org/10.3390/polym15143005.

Lopes, H., Silva, S., Machado, J., 2020. Analysis of the effect of shape factor on cork–rubber composites under small strain compression. Appl. Sci. 10, 7177. https://doi.org/10.3390/app10207177.

Mathworks fmincon documentation, (n.d.). https://es.mathworks.com/help/optim/ug/fmincon.html (accessed September 22, 2025).

Modela MDX-40A 3D milling machine | roland DGA, roland website (n.d.). https://www.rolanddga.com/es-la/soporte/products/milling/modela-mdx-40a-3d-milling-machine (accessed February 6, 2025).

Modular compact rheometer: MCR 102e/302e/502e, Anton Paar (n.d.). https://www.anton-paar.com/corp-en/products/details/rheometer-mcr-102-302-502/(accessed March 25, 2025).

Müller-Pabel, M., Rodríguez Agudo, J.A., Gude, M., 2022. Measuring and understanding cure-dependent viscoelastic properties of epoxy resin: a review. Polym. Test. 114, 107701. https://doi.org/10.1016/j.polymertesting.2022.107701.

Nashif, A.D., Jones, D.I.G., Henderson, J.P., 1985. Vibration Damping. J. Wiley and sons, New York Chichester Brisbane [etc.

Pal, S., Bhattacharyya, A., 2025. Measurement of axial and shear mechanical response of PDMS elastomers and determination of Poisson's ratio using digital image correlation. Polym. Test. 143, 108687. https://doi.org/10.1016/j.polymertesting.2025.108687.

Pattison, A.J., McGarry, M., Weaver, J.B., Paulsen, K.D., 2015. A dynamic mechanical analysis technique for porous media. IEEE Trans. Biomed. Eng. 62, 443–449. https://doi.org/10.1109/tbme.2014.2357771.

Phansalkar, S.P., Mittakolu, R., Han, B., Kim, T., 2025. Enhanced DMA test procedure to measure viscoelastic properties of epoxy-based molding compound: multiple oscillatory strain amplitudes and monotonic loading. Micromachines 16, 384. https://doi.org/10.3390/mi16040384.

Pritz, T., 1998. Frequency dependences of complex moduli and complex poisson's ratio of real solid materials. J. Sound Vib. 214, 83–104. https://doi.org/10.1006/jsvi.1998.1534.

Pritz, T., 2000. Measurement methods of complex Poisson's ratio of viscoelastic materials. Appl. Acoust. 60, 279–292. https://doi.org/10.1016/S0003-682X(99)00049-3.

Pritz, T., 2007. The Poisson's loss factor of solid viscoelastic materials. J. Sound Vib. 306, 790–802. https://doi.org/10.1016/j.jsv.2007.06.016.

Rodríguez Agudo, J.A., Haeberle, J., Müller-Pabel, M., Troiss, A., Shetty, A., Kaschta, J., Giehl, C., 2023. Characterization of the temperature and frequency dependency of the complex Poisson's ratio using a novel combined torsional-axial rheometer. J. Rheol. 67, 1221–1250. https://doi.org/10.1122/8.0000675.

Sim, S., Kim, K.-J., 1990. A method to determine the complex modulus and poisson's ratio of viscoelastic materials for FEM applications. J. Sound Vib. 141, 71–82. https://doi.org/10.1016/0022-460X(90)90513-Y.

Smith, A.M., Inocencio, D.G., Pardi, B.M., Gopinath, A., Andresen Eguiluz, R.C., 2024. Facile determination of the poisson's ratio and young's modulus of polyacrylamide gels and polydimethylsiloxane. ACS Appl. Polym. Mater. 6, 2405–2416. https://doi.org/10.1021/acsapm.3c03154.

Somanath, S., Marimuthu, R., Krishnapillai, S., 2023. Frequency domain analysis of pre-stressed elastomeric vibration isolators. Def. Technol. 25, 33–47. https://doi.org/10.1016/j.dt.2022.10.004.

Sousa, T.L.D., Silva, J.D., Pereira, J.T., 2018. Indirect identification of the complex poisson's ratio in fractional viscoelasticity. Lat. Am. J. Solid. Struct. 15. https://doi.org/10.1590/1679-78254920.

Szabó, B.A., Babuška, I., 2021. Finite Element Analysis: Method, Verification and Validation, second ed. Wiley, Hoboken, NJ.

Tschoegl, N.W., Knauss, W.G., Emri, I., 2002. Poisson's Ratio in Linear Viscoelasticity – a Critical Review.

Vatandoost, H., Hemmatian, M., Sedaghati, R., Rakheja, S., 2021. Effect of shape factor on compression mode dynamic properties of magnetorheological elastomers. J. Intell. Mater. Syst. Struct. 32, 1678–1699. https://doi.org/10.1177/1045389X20983921.

Virág, Á.D., Juhász, Z., Kossa, A., Molnár, K., 2024. Combining oscillatory shear rheometry and dynamic mechanical analysis to obtain wide-frequency master curves. Polymer 295, 126742. https://doi.org/10.1016/j.polymer.2024.126742.

Walter, B.L., Pelteret, J.-P., Kaschta, J., Schubert, D.W., Steinmann, P., 2017a. On the wall slip phenomenon of elastomers in oscillatory shear measurements using parallel-plate rotational rheometry: I. Detecting wall slip. Polym. Test. 61, 430–440. https://doi.org/10.1016/j.polymertesting.2017.05.035.

Walter, B.L., Pelteret, J.-P., Kaschta, J., Schubert, D.W., Steinmann, P., 2017b. On the wall slip phenomenon of elastomers in oscillatory shear measurements using parallel-plate rotational rheometry: II. Influence of experimental conditions. Polym. Test. 61, 455–463. https://doi.org/10.1016/j.polymertesting.2017.05.036.

Wang, B., Kari, L., Pang, H., Gong, X., 2024. Modelling the dynamic magnetic actuation of isotropic soft magnetorheological elastomers. Int. J. Mech. Sci. 266, 108908. https://doi.org/10.1016/j.ijmecsci.2023.108908.

Xu, X., Gupta, N., 2018. Determining elastic modulus from dynamic mechanical analysis: a general model based on loss modulus data. Materialia 4, 221–226. https://doi.org/10.1016/j.mtla.2018.09.034.

Yaghoobi, A., Jalali, A., Norouzi, M., Ghatee, M., 2022. Aspect ratio dependency of magneto-rheological elastomers in dynamic tension-compression loading. IEEE Trans. Magn. 58, 1–13. https://doi.org/10.1109/TMAG.2022.3152031.

Yang, L., Ou, Z., Jiang, G., 2023. Research progress of elastomer materials and application of elastomers in drilling fluid. Polymers 15, 918. https://doi.org/10.3390/polym15040918.

Zhao, Z., Chen, Y., Hu, X., Bao, R., Wu, B., Chen, W., 2023. Vibrations and waves in soft dielectric elastomer structures. Int. J. Mech. Sci. 239, 107885. https://doi.org/10.1016/j.ijmecsci.2022.107885.

Zhu, X., Li, W., 2021. Research on dynamic compression testing of silicone rubber under different temperatures. J. Phys.: Conf. Ser. 2002, 012047. https://doi.org/10.1088/1742-6596/2002/1/012047.